Applied Physics Letters

RESEARCH ARTICLE | JUNE 09 2023

High sensitivity multiscale and multitasking terahertz Janus sensor based on photonic spin Hall effect FREE

Jun-Yang Sui ; Jia-Hao Zou ; Si-Yuan Liao ; Bing-Xiang Li ; Hai-Feng Zhang

Appl. Phys. Lett. 122, 231105 (2023)
https://doi.org/10.1063/5.0153342

Applied Physics Letters ARTICLE pubs.aip.org/aip/apl

High sensitivity multiscale and multitasking terahertz Janus sensor based on photonic spin Hall effect

Cite as: Appl. Phys. Lett. **122**, 231105 (2023); doi: 10.1063/5.0153342
Submitted: 6 April 2023 · Accepted: 25 May 2023 ·
Published Online: 9 June 2023

Jun-Yang Sui, Jia-Hao Zou, Si-Yuan Liao, Bing-Xiang Li,[a] and Hai-Feng Zhang[a]

AFFILIATIONS

College of Electronic and Optical Engineering & College of Flexible Electronics (Future Technology), Nanjing University of Posts and Telecommunications, Nanjing 210023, China

[a]Authors to whom correspondence should be addressed: bxli@njupt.edu.cn and hanlor@163.com or hanlor@njupt.edu.cn

ABSTRACT

Photonic spin Hall effect (PSHE) is an effective metrological tool to characterize the variation in weak refractive index (RI) and nanostructure parameters. In this Letter, a highly sensitive terahertz Janus sensor (JS) based on PSHE is proposed. Through the asymmetric arrangement of different dielectrics, the sensor has a Janus feature, realizing the multitasking of thickness and RI detection on multiple scales. When electromagnetic waves (EWs) are incident into the JS from the forward scale, the number of graphene layers (1–7 layers) can be exactly identified by thickness detection. Enhancing the PSHE by the property of graphene, the JS can extend the thickness change of the graphene layer at the nanometer level by 10^6 times to the millimeter level with a sensitivity of 3.02×10^{-3} m/nm. In the case of EWs backward scale propagation, based on the sensitivity of 6.244×10^{-3} m/RIU, the JS can identify different kinds of waterborne bacterium such as *Vibrio cholerae*, *Escherichia coli*, and *Shigella flexneri*, in the RI range of 1.355–1.43 with high precision. The design of the multiscale and multitasking JS with high sensitivity is of great significance for accelerating the research and exploration of graphene materials. In addition, it provides an idea for real-time, no-label, and low-cost detection in the biomedical field.

Terahertz (THz) spectroscopy is defined as the frequency scope of electromagnetic waves (EWs) from 0.1 to 10 THz. Due to the advantages of nondestructive, penetrating, unmarked, and real-time detection,[1] THz detection has laid a foundation for many applications in industrial film production and biomedical detection.[2,3] Photonic spin Hall effect (PSHE) is characterized by splitting of transverse spin that occurs when a light beam with limited space passes from one material to another with a different refractive index (RI),[4] which is the photon version of the spin Hall effect in electronic systems. Spin migration in the PSHE is very sensitive to changes in the physical parameters of the system, so it can be used as an accurate measurement tool to characterize changes in weak RI and nanostructure parameters.[5] Fortunately, Hosten *et al.*[6] proposed a weak measurement technique, which magnified the PSHE phenomenon observed in the experiment by nearly 10^4 times, making it more convenient to measure the change in physical quantities. Recently, Dong *et al.*[7] demonstrated that the introduction of a graphene monolayer into silicon aerogel could significantly improve the PSHE in the THz region. In addition, some scholars have proposed that PSHE could be effectively enhanced and regulated by graphene[8,9] or silicon,[10,11] which was able to be adjusted by external electric or magnetic fields, achieving excellent results. These findings suggest ways to improve the PSHE in the THz band.

Due to the excellent properties such as strong conductivity, high carrier mobility, and good thermal conductivity, graphene thin films have potential applications in electronic materials, heat dissipation materials, and biomedicine fields.[12] How quickly and easily identifying the number of graphene layers is significant to accelerate the research and exploration of graphene materials.[13] However, there are many ways to determine the number of graphene layers, but they all have limitations. For instance, the most straightforward method is the atomic force microscopy technique, but it shows a sluggish throughput and has the potential to cause harm to the sample. The unconventional quantum Hall effect is often used to distinguish among single, double, and multilayered graphene,[14] and Raman spectroscopy can quickly and nondestructively measure the layers of graphene.[15] However, the difference between double and multilayered graphene films is not obvious, which is prone to error. Therefore, improving the

TABLE I. The multitasking detection performance of the Janus sensor (JS).

Forward	Thickness detection	Range	0.34–2.38 nm
		S	3.02×10^{-3} m/nm
Backward	RI detection	Range	1.365–1.422
		S	6.235×10^{-3} m/RIU

sensitivity (S) of graphene layer number detection under the condition of fast response speed and without damaging the sample has become a research focus. Water safety is a major concern, especially in densely populated cities, where pathogenic microorganisms in drinking water, such as *Vibrio cholerae*, *Escherichia coli* (*E. coli*), and *Shigella flexneri*, are potential causes of deadly outbreaks.[16] To date, preventing outbreaks of waterborne bacteria remains a severe challenge for global drinking water supplies. Although we have existing some traditional bacterial detection techniques that can diagnose many pathogens in drinking water,[17] these methods are time-consuming, requiring 18–72 h for the pathogen to grow to a quantifiable concentration, so they cannot meet the requirements for field water quality testing. In addition, these traditional techniques have the problems of low S and poor specificity. Therefore, to effectively avoid bacterial outbreaks, biosensors with high S, small size, low cost, and real-time detection are more than indispensable and necessary.

In this Letter, inspired by the creation god Janus with two different faces in Roman mythology,[18] through the asymmetric arrangement of different dielectrics, the layered structure that realizes different detection tasks on multiple scales is called the Janus sensor (JS). Due to the integration of multitasking, the JS proposed not only saves the extra cost required by multiple diverse single-function sensors to complete the tasks but also expands the research direction of sensors, which only focuses on performance improvement in the past.[19] The JS is designed to have a detection cavity in the middle, when the EWs propagate from different directions, the different analytes will be placed inside. Utilizing the PSHE displacement δ_+^H, the 1–7 graphene layers (thickness 0.34–2.38 nm) can be accurately detected on the forward scale with $S = 3.02 \times 10^{-3}$ m/nm. On the backward scale, by locating the δ_+^H peak value, *V. cholerae* (an RI of 1.365), *E.coli* (an RI of 1.388), and *Shigella flexneri* (an RI of 1.422) can be identified by RI detection with $S = 6.235 \times 10^{-3}$ m/RIU. The use of different frequencies in the front ($f = 5.0403$ THz) and rear ($f = 0.531$ THz) EWs also reflects the advantages of wavelength division multiplexing. Table I shows the excellent sensing performance of the proposed THz JS with the advantages of small size, high S, fast response, and nondestructive, indicating that it has potential applications in engineering applications and biomedical detection, which owns a certain research value.

The layered structure corresponding to the JS is shown in Fig. 1(a), in which a cavity (RI of 1) is set as the detection cavity ($d_{\text{cavity}} = 10\ \mu$m). For fabrication of the layered structure, Guo *et al.* outlined the etching method, which can be referred to Ref. 20 (supplementary material section 1 provides the method). Since theoretical research is the key to this Letter, experimental verification is not within the scope of this article. The JS is exposed to air and operates at 300 K to adapt to ordinary conditions. Red and blue lines represent EWs incident forward and backward, respectively. In the case of EWs forward propagation, the thin Teflon film ($n_{\text{Teflon}} = 1.46$)[21] with a thickness of $d_{\text{Teflon}} = 4\ \mu$m is inserted into the center of the detection cavity as the sample holding place.[21] The graphene to be detected (the thickness is d_{gt}) can be loaded on one side of the Teflon film [as displayed in Fig. 1(b)] for thickness detection. On the backward scale, a precise technique that employs hollow sub micrometer size pipettes based on micro-infiltration technology is utilized to inject the waterborne bacterium to be detected [as exhibited in Fig. 1(c)] into the detection cavity for RI detection.[22] The thicknesses of ordinary dielectrics A, B, and graphene monolayer are $d_A = 3\ \mu$m, $d_B = 8\ \mu$m, and $d_g = 0.34$ nm, respectively. It is worth highlighting that Leiwin[23] based on the Mie resonance theory deduced an expression for effective permittivity and permeability

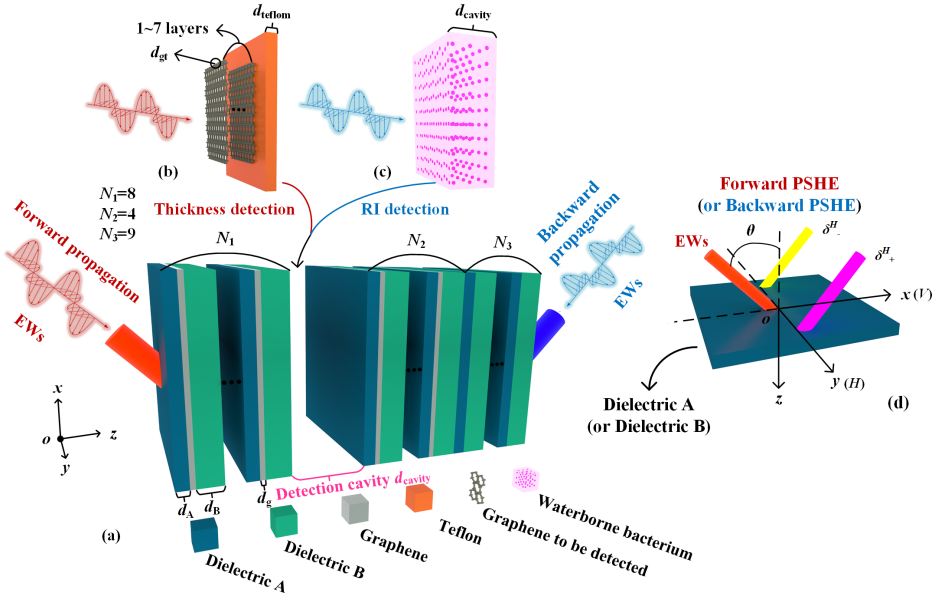

FIG. 1. Schematic diagram of the JS layered structure. (a) The overall structure is composed of different dielectrics arranged asymmetrically, $(AGB)^8$Cavity(AGB)4(AB)9, where the G and Cavity separately symbolize the graphene and detection cavity, respectively. Additionally, EWs propagate from the forward and backward directions. (b) The graphene detected for layer number is loaded on the one side of the Teflon film. (c) The waterborne bacterium is to be detected. (d) The PSHE phenomena of incident EWs occurring at the first-layer dielectric interfaces belong to the forward or backward scale.

of composite materials, enabling the achievement of desired RI over a wide range, and this technique has been applied in practice.[24] Therefore, the RI of ordinary dielectrics A and B are $n_A = 2.4$ and $n_B = 4.1$, which is reasonable and can be obtained in practice. The permittivity of the graphene is a function of the surface conductivity σ, which is composed of intraband σ_{intra} and interband σ_{inter} (details can be seen in supplementary material section 2),[25]

$$\sigma = \frac{ie^2 k_B T}{\pi\hbar^2(\omega + i/\tau)}\left(\frac{\mu_C}{k_B T} + 2\ln\left(e^{-\frac{\mu_C}{k_B T}} + 1\right)\right) + \frac{ie^2}{4\pi\hbar}\ln\left|\frac{2\mu_C - \hbar(\omega + i/\tau)}{2\mu_C + \hbar(\omega + i/\tau)}\right|, \quad (1)$$

where ω, $\hbar$, k_B, e, T, μ_C, and τ severally correspond to the angular frequency, Planck constant, Boltzmann constant, electron charge, chemical potential, and relaxation time, respectively. Relaxation time τ is set to 1×10^{-13} s.

Figure 1(d) shows the PSHE phenomena generated at the dielectric interfaces on the forward or backward scale of a sufficiently narrow Gaussian beam with a certain incidence angle θ. The purple and yellow beams separately symbolize the left-hand and right-hand circularly polarized components reflected at the interface. It can be expressed as a local wave packet with an arbitrary narrow spectrum,[26]

$$\tilde{E}i\pm = (eix + ioeiy)\frac{\omega_0}{\sqrt{2\pi}}\exp\left[-\frac{\omega_0^2(k_{ix}^2 + k_{iy}^2)}{4}\right], \quad (2)$$

where ω_0 symbolizes the beam waist, o is the polarization operator, and the left-handed and right-handed circularly polarized beams are severally represented by $o = 1$ and $o = -1$. H and V are, respectively, used to denote the horizontally and vertically polarized states, which are set along the $+y$-axis and $+x$-axis [exhibited in Fig. 1(d)]. To obtain the reflected field, the relationship between the incident field and the reflected field is needed to be established,[26]

$$pt\begin{bmatrix}\tilde{E}_r^H \\ \tilde{E}_r^V\end{bmatrix} = \begin{bmatrix} r^p & \frac{kry\cot\theta_i(r^p + r^s)}{k_0} \\ -\frac{kry\cot\theta_i(r^p + r^s)}{k_0} & r^s\end{bmatrix}\begin{bmatrix}\tilde{E}_i^H \\ \tilde{E}_i^V\end{bmatrix}, \quad (3)$$

where k_0 is the wave number in free space. The Fresnel reflection coefficients of s and p waves are expressed as r^s and r^p (detailed calculations can be seen in supplementary material section 3), where the electric field vectors of s and p waves are set along the $+y$-axis and $+x$-axis, respectively. According to Eqs. (2) and (3), we can obtain the expression of the reflection angle spectrum,[26]

$$\tilde{E}_r^H = \frac{r^p}{\sqrt{2}}\left[\exp\left(+ik_{ry}\delta_r^H\right)\tilde{E}_{r+} + \exp\left(-ik_{ry}\delta_r^H\right)\tilde{E}_{r-}\right], \quad (4)$$

$$\tilde{E}_r^V = \frac{ir^s}{\sqrt{2}}\left[-\exp\left(+ik_{ry}\delta_r^V\right)\tilde{E}_{r+} + \exp\left(-ik_{ry}\delta_r^V\right)\tilde{E}_{r-}\right]. \quad (5)$$

Here, $\delta^H{}_r = (1 + r^s/r^p)\cot\theta_i/k_0$ and $\delta^V{}_r = (1 + r^p/r^s)\cot\theta_i/k_0$. $\tilde{E}_{r\pm}$ can be written in a similar style to Eq. (2). For reflected light, the lateral displacement of the two spin components of the PSHE can be expressed as[26]

$$\delta_\pm^H = \mp\frac{\lambda}{2\pi}\left[1 + \frac{|r^s|}{|r^p|}\cos(\varphi^s - \varphi^p)\right]\cot\theta_i, \quad (6)$$

$$\delta_\pm^V = \mp\frac{\lambda}{2\pi}\left[1 + \frac{|r^p|}{|r^s|}\cos(\varphi^p - \varphi^s)\right]\cot\theta_i. \quad (7)$$

In this Letter, we only discuss the displacement δ_+^H of the left-handed circularly polarized component under horizontal polarization of PSHE.

To elucidate the origin of the δ_+^H peak and the selection of the graphene chemical potential μ_C, the thickness detection of one graphene layer ($d_{gt} = 0.34$ nm) on the forward scale with EWs $f = 5.0403$ THz is taken as an example. The graphene to be detected is consistent with the μ_C of the graphene monolayer in the layered structure. μ_C is regulated by an external voltage, and Qi *et al.*[27] proposed an experimental approach for altering the μ_C of graphene (supplementary material section 4 gives the method that the experimental adjustment of μ_C). As shown in Fig. 2, the real and imaginary parts of the graphene surface conductivity σ increase gradually with the μ_C rising in the range of 0.2–0.8 eV, which is consistent with Eq. (1). The variation of graphene σ will adjust the effective RI and impedance of the entire layered structure, thus affecting the wave vector and phase of the EWs propagating in it, which is reflected in the reflection coefficient as displayed in Fig. 3.[28] Four standard values of μ_C are selected as 0.2, 0.4, 0.6, and 0.8 eV. Figure 3 shows the corresponding relation curves of $|r^s|$, $|r^p|$, and θ. The Fresnel reflection coefficients for p and s waves, denoted by $|r^s|$ and $|r^p|$, are represented by solid red lines and dashed blue lines. As exhibited in Figs. 3(a)–3(d), with the increase in μ_C at an equal interval of 0.2 eV, $|r^s|$ and $|r^p|$ curves change accordingly. It is found that at a certain θ, $|r^s|$ and $|r^p|$ will decline rapidly, and the lowest values of $|r^p|$ are 0.11, 0.09, 1.29×10^{-4}, and 0.11. This is due to the introduction of the defect layer, which makes the energy localized, thus, generating the reflection gap and forming the defect peak. The corresponding θ also decreases gradually. According to the beam displacement of Eq. (6), the magnitude of the PSHE displacement mainly depends on the $|r^s|/|r^p|$ portion, so $|r^s|/|r^p|$ reaches its maximum near the defect peak of $|r^p|$, thus obtaining the peak value of δ_+^H.[28] This theory is further verified more clearly in Fig. 4. Figures 4(a) and 4(b) show the δ_+^H values at different μ_C. With the increase in μ_C, δ_+^H peaks at θ of 64.06°, 58.31°, 55.85°, and 46.6° separately possess values of

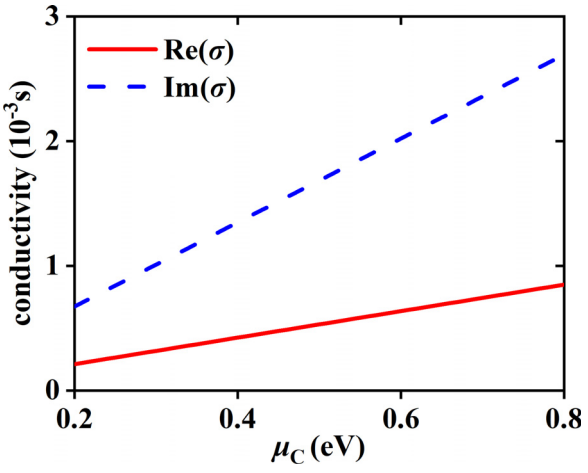

FIG. 2. The real and imaginary parts of the graphene surface conductivity σ under different μ_C.

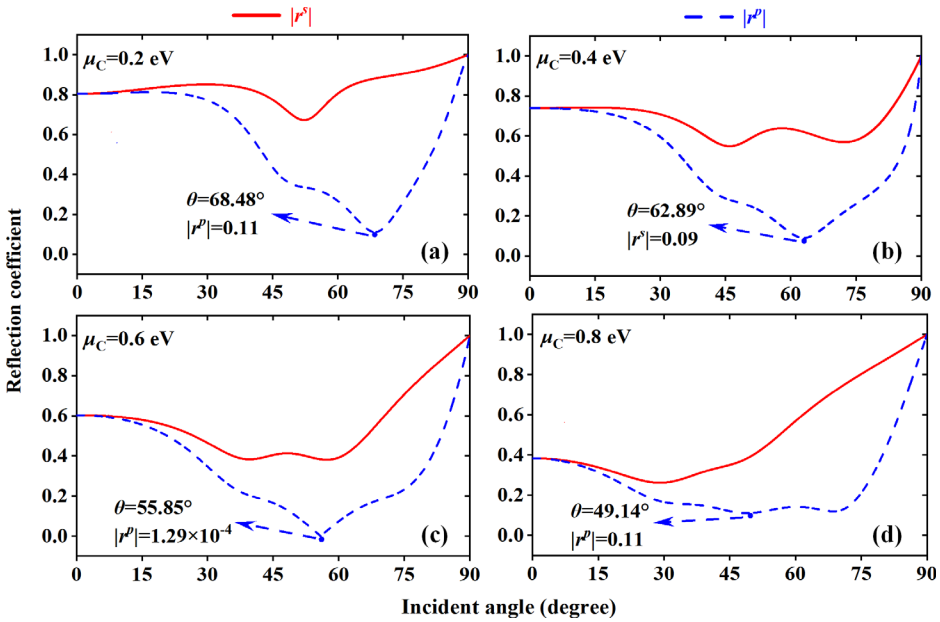

FIG. 3. The reflection coefficient curves of $|r^s|$ and $|r^p|$ with different μ_C, (a) $\mu_C = 0.2$ eV, (b) $\mu_C = 0.4$ eV, (c) $\mu_C = 0.6$ eV, (d) and $\mu_C = 0.8$ eV.

1.2×10^{-5}, 1.47×10^{-5}, 1.38×10^{-2}, and 1.71×10^{-5} m, respectively. It is found that the maximum value of δ_+^H at $\mu_C = 0.6$ eV is about 10^3 times higher than that at other μ_C, reaching the millimeter range, which is consistent with the $|r^p|$ has a minimum value of 1.29×10^{-4} compared with other μ_C value cases in Fig. 3(c). (The physical analysis of the δ_+^H enhancement in the millimeter range is shown in supplementary material section 5.)[29,30] Figure 4(c) exhibits the variation of δ_+^H peak values with the increase in the graphene layers number ($d_{gt} = 0.34$–1.7 nm) under different selected μ_C values. The peak value of δ_+^H at $\mu_C = 0.6$ eV is significantly higher than in other cases and changes significantly with the change of d_{gt}. Because the JS proposed achieves forward scale thickness and backward scale RI detection by locking the peak value of δ_+^H, selecting $\mu_C = 0.6$ eV can obtain better detection performance.

When EWs are incident into the JS at a frequency of $f = 5.0403$ THz (the selection of the forward incident frequency is

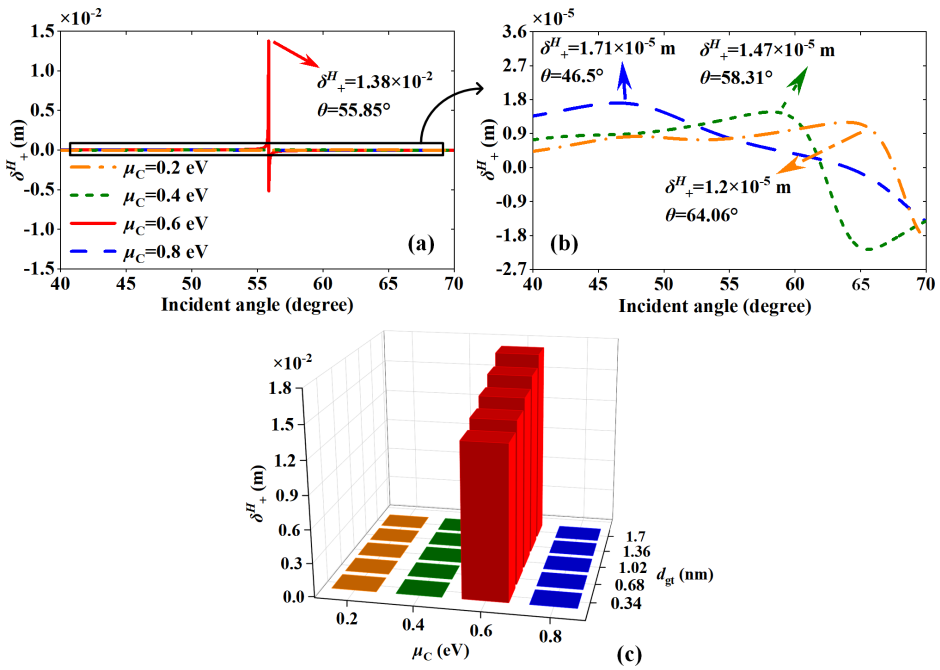

FIG. 4. When μ_C changes and EWs are incident from the forward direction, (a) the comparison plots of δ_+^H under $d_{gt} = 0.34$ nm, (b) and the enlarged image. (c) Plots of δ_+^H peak values under different d_{gt}.

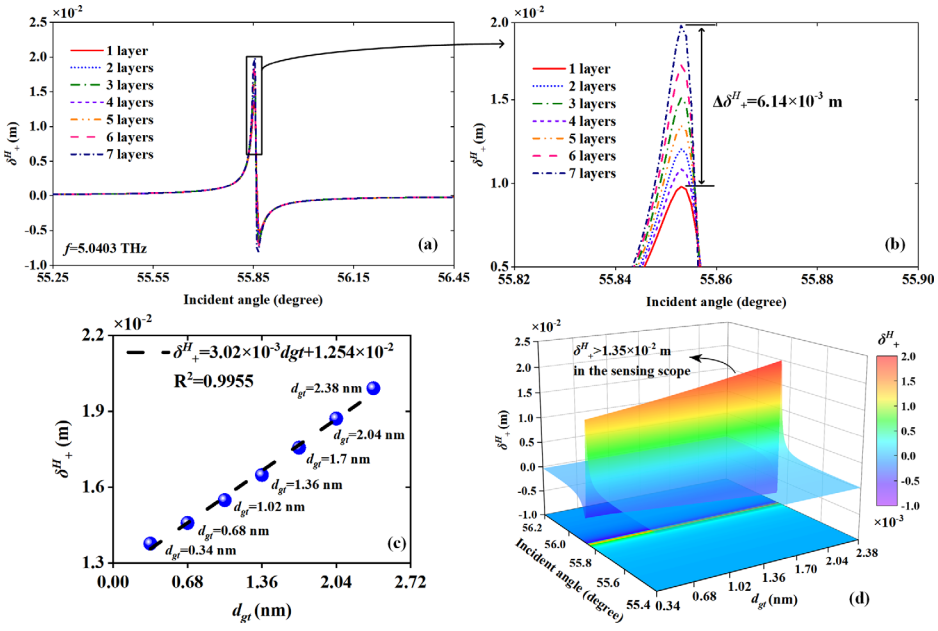

FIG. 5. Schematic diagrams of the thickness detection when EWs propagate forward. (a) The δ_+^H peaks belonging to 1–7 layers number of graphene and (b) the enlarged image. (c) The LFR between δ_+^H and d_{gt}. (d) Continuous varying δ_+^H peaks.

explained in supplementary material section 6), the JS provides a simple and convenient way to accurately determine the graphene layers number without damaging the sample. The thin Teflon film ($d_{teflon} = 4\,\mu m$) is placed in the center of the detection cavity ($d_{cavity} = 10\,\mu m$), and the distances between the Teflon film and both sides of the detection cavity are equal to $3\,\mu m$. When the graphene layers to be detected are loaded on the one side of the thin Teflon film as shown in Fig. 1(b) for thickness detection, the remaining space of the detection cavity is air with the RI of 1, whose stable property will not interfere with the calculation. Similar to the principle of δ_+^H variation caused by μ_C, the diverse number of graphene layers, namely, the different thickness d_{gt}, will cause the optical path change of EWs propagation in the layered structure, which will also affect the adjustment of wave vector and phase, and then alters the Fresnel reflection coefficients $|r^s|$ and $|r^p|$. Hence, as indicated in Fig. 5(a), the peak values of δ_+^H vary with the number of graphene layers. With an increase in the number of graphene layers from 1 to 7 (d_{gt} of 0.34, 0.68, 1.02, 1.36, 1.7, 2.04, and 2.38 nm), the corresponding δ_+^H peaks at the $\theta = 55.85°$ are 1.38×10^{-2}, 1.46×10^{-2}, 1.55×10^{-2}, 1.65×10^{-2}, 1.76×10^{-2}, 1.87×10^{-2}, and 1.99×10^{-2} m, respectively. Figure 5(b) displays that the difference between the minimum and maximum δ_+^H values is up to $\Delta\delta_+^H = 6.14 \times 10^{-3}$ m, manifesting that δ_+^H is highly responsive to d_{gt}. To more clearly display the detection performance of the JS, the detection points are taken with an equal spacing of 0.34 nm between 0.34 and 2.38 nm, and the linear fitting method is utilized to obtain the linear fitting relation (LFR). Figure 5(c) shows the LFR of δ_+^H and d_{gt}, which is $\delta_+^H = 3.02 \times 10^{-3} d_{gt} + 1.254 \times 10^{-2}$. 3.02×10^{-3} m/nm is the S, indicating that the JS can enlarge the thickness variation of graphene at the nanometer level by 10^6 times through the PSHE and reasonable layered structure design, which reaches the sensitive response at the millimeter level. R^2 is used to evaluate the quality of linear fitting, and $R^2 = 0.9955$ proves the reliability of the JS thickness detection. Compared with Zhou *et al.*[31] using the change of the PSHE displacement peak at a micrometer level to measure 1–5 layers of graphene, the PSHE displacement peak values in this Letter up to the centimeter level improve the accuracy and convenience of experimental observation and also increase the detection layers number of graphene. Figure 5(d) exhibits the variation of δ_+^H when d_{gt} changes continuously in the range of 0.34–2.38 nm at an equal interval of 1×10^{-3} nm. In this detection range, the δ_+^H peaks are all greater than 1.35×10^{-2} m and linearly rise with increasing d_{gt}, indicating that the δ_+^H peak value can be locked to accurately detect the graphene thickness range in this scope by LFR, which has important implications for future graphene research.

Table II shows the RI corresponding to single waterborne bacteria of *V. cholerae*, *E. coli*, and *S. flexneri* detected by the immersion refraction method using a phase contrast microscope.[32] As the RI of bacteria is dependent on the mass density of the internal components like protein concentration, nuclear contents, and cell sub organelles, it may be a unique parameter to distinguish different bacterial species.[33]

When EWs propagate on the backward scale at a frequency of 0.531 THz (the selection of the backward incident frequency is explained in supplementary material section 6), the waterborne bacterium to be detected is injected into the detection cavity.[22] By locking the δ_+^H peak, the proposed JS can detect *V. cholera*, *E. coli*, and *S. flexneri* with high precision. Figure 6(a) exhibits the δ_+^H peaks belonging to RI (n_{wb}) of different waterborne bacteria species. With the increase in n_{wb}, the δ_+^H peaks gradually rise. The peak values are separately

TABLE II. Three different species of waterborne bacteria and their RI.[32] Reproduced with permission from Liu *et al.*, Lab Chip. 14, 4237–4243 (2014). Copyright 2014 Royal Society of Chemistry.

Waterborne bacteria	*V. cholera*	*E. Coli*	*S. flexneri*
RI	1.365	1.388	1.422

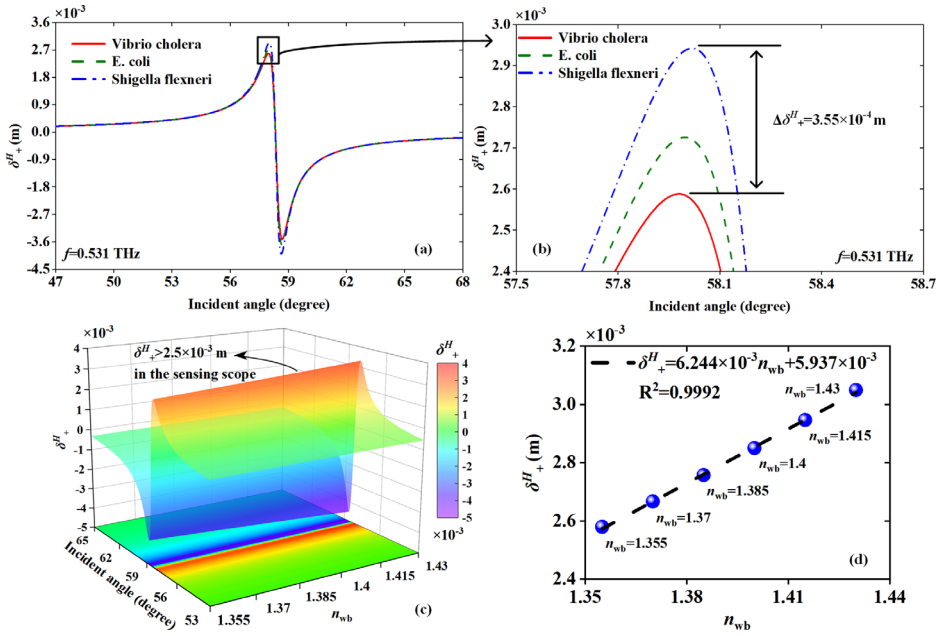

FIG. 6. Schematic diagrams of the RI detection when EWs propagate backward. (a) The δ_+^H peaks belong to three species of waterborne bacteria, (b) and the enlarged image. (c) The LFR between δ_+^H and n_{wb}. (d) Continuously varying δ_+^H peaks.

taken as 2.59×10^{-3}, 2.73×10^{-3}, and 2.94×10^{-3} m. The difference between minimum and maximum peak values indicated in Fig. 6(b) is $\Delta\delta_+^H = 3.55 \times 10^{-4}$. Figure 6(c) shows the continuous variation of δ_+^H in the range of 1.355–1.43 when RI varies with the equivalent value of 10^{-4} RIU. Within the detection range, $\delta_+^H > 2.5 \times 10^{-3}$ m, which meets the requirement of the detection peak value. According to the red line of the projection region of the three-dimensional diagram, the δ_+^H peaks under different RI always correspond to the EWs incident angle θ of 58.02°, which facilitates the detection of the maximum SPHE displacement value in the experiment. To confirm the superior performance of RI detection, the LFR of detection points, which are taken at 0.015 RIU intervals within the RI range of 1.355–1.43, is presented in Fig. 6(d). The LFR is $\delta_+^H = 6.244 \times 10^{-3}\, n_{wb} - 5.937 \times 10^{-3}$ with $S = 6.244 \times 10^{-3}$ m/RIU and $R^2 = 0.9992$, indicating that the RI detection of the JS is sensitive and reliable. The detection scope of RI completely covers the RI of the three waterborne bacterium.[32] Additionally, other bacteria with RI in the range of 1.355–1.43 can also be accurately detected with a resolution of up to 1×10^{-4} RIU. (Details are exhibited in supplementary material section 7.) Compared with the low resolution of 10^{-2} RIU by digital holographic microscopy and light scattering[34,35] and the minimum detectable RI difference of 5×10^{-3} RIU by the immersion refraction method,[32] the detection accuracy of the proposed JS is higher. Due to the low quantum energy and high stability of THz waves, the JS with small size and low cost will not destroy bacterial samples and can be used for water quality detection in the field scene. Meanwhile, it also has a high potential application in the detection of pathogens in the food and clinical industry.

In conclusion, this Letter proposed a multiscale and multitasking JS based on the PSHE in the THz band, which can achieve accurate thickness detection and RI detection on two different scales. Compared with the previously reported work, the JS proposed in this Letter has made innovations and breakthroughs, and its overall performance is better. (The comparison table is in Sec. 8 of the supplementary material.) The multitasking integration of the JS can effectively reduce the cost of requiring multiple single-function sensors. The PSHE displacement δ_+^H can be effectively enhanced by designing a reasonable layered structure and regulating the μ_C of graphene. By locking δ_+^H peak values, 1–7 layers of graphene can be detected on the forward scale with $S = 3.02 \times 10^{-3}$ m/nm, and the thickness variation at the nanometer level is amplified by 10^6 times to reach the millimeter level, which improves the S and accuracy of experimental observation. On the backward scale, when different waterborne bacteria are injected into the detection cavity, the species of the waterborne bacterium can be easily identified by RI detection with $S = 6.244 \times 10^{-3}$ m/RIU via the peak value of δ_+^H. The JS based on the THz band with small size, nondestructive, penetration, no mark, real-time detection, and stability has broad application prospects in industrial production, biomedicine, and other fields.

See the supplementary material for supporting content.

This work was supported by the National Key Research and Development Program of China (Grant No. 2022YFA1405000), the Natural Science Foundation of Jiangsu Province, the Major Project (Grant No. BK20212004), the Natural Science Research Start-up Foundation of Recruiting Talents of Nanjing University of Posts and Telecommunications (Grant No. NY222105), and the National College Students Innovation and Entrepreneurship Training Program (Grant No. 202210293014Z).

AUTHOR DECLARATIONS

Conflict of Interest

The authors have no conflicts to disclose.

Author Contributions

Jun-Yang Sui: Investigation (lead); Validation (lead); Writing – original draft (lead). **Jia-Hao Zou:** Software (lead); Visualization (lead). **Si-Yuan Liao:** Data curation (lead); Investigation (supporting). **Bing-Xiang Li:** Funding acquisition (equal); Validation (equal); Writing – review & editing (equal). **Hai-Feng Zhang:** Conceptualization (equal); Writing – review & editing (equal).

DATA AVAILABILITY

The data that support the findings of this study are available from the corresponding authors upon reasonable request.

REFERENCES

[1]W. J. Choi, K. Yano, M. Cha, F. M. Colombari, J. Y. Kim, Y. Wang, S. H. Lee, K. Sun, J. M. Kruger, A. F. de Moura, and N. A. Kotov, Nat. Photonics **16**, 366–373 (2022).
[2]J. F. O'Hara, W. Withayachumnankul, and I. Al-Naib, J Infrared Milli Terahz Waves **33**, 245–291 (2012).
[3]H. B. Liu, Y. Chen, G. J. Bastiaans, and X. C. Zhang, Opt. Express **14**, 415–423 (2006).
[4]K. Y. Bliokh, and Y. P. Bliokh, Phys. Rev. Lett. **96**, 073903 (2006).
[5]S. Chen, X. Zhou, and X. Ling, Appl. Phy. Lett. **118**, 111104 (2021).
[6]O. Hosten and P. Kwiat, Science **319**, 787–790 (2008).
[7]P. Dong, J. Cheng, H. Da, and X. Yan, Opt. Commun. **485**, 126744 (2021).
[8]M. Shah, Opt. Mater. Express **12**, 421–435 (2022).
[9]X. Bai, L. Tang, W. Lu, X. Wei, S. Liu, Y. Liu, X. Sun, H. Shi, and Y. Lu, Opt. Lett. **42**, 4087–4090 (2017).
[10]M. Shah and M. S. Anwar, Phys. Lett. A **401**, 127342 (2021).
[11]M. Shah, J. Phys. D: Appl. Phys. **55**, 105105 (2022).
[12]S. Luo, X. Chen, and Y. He, J. Mater. Chem. B **9**, 6129–6143 (2021).
[13]A. K. Geim, Science **324**, 1530–1534 (2009).
[14]Y. Zhang, Y. W. Tan, H. L. Stormer, and P. Kim, Nature **438**, 201–204 (2005).
[15]A. Gupta, G. Chen, P. Joshi, S. Tadigadapa, and Eklund, Nano Lett. **6**, 2667–2673 (2006).
[16]R. Lopez-Roldan, P. Tusell, J. L. Cortina, S. Courtois, and J. L. Cortina, TrAC Trends Anal. Chem. **44**, 46–57 (2013).
[17]L. Zeng, L. Wang, and J. Hu, Biosensing Technologies for the Detection of Pathogens **73178**, 6–19 (2018).
[18]C. Chen, X. Ye, J. Sun, Y. Chen, C. Huang, X. Xiao, W. Song, S. Zhu, and T. Li, Optica **9**, 1314–1322 (2022).
[19]P. Dong, J. Cheng, and H. Da, New J. Phys. **22**, 113007 (2020).
[20]S. Guo, C. Hu, and H. Zhang, J. Opt. **22**, 105101 (2020).
[21]X. Shi and Z. Han, Sci. Rep. **7**, 13147 (2017).
[22]F. Intonti, S. Vignolini, V. Türck, M. Colocci, P. Bettotti, L. Pavesi, S. L. Schweizer, R. Wehrspohn, and D. Wiersma, Appl. Phys. Lett. **89**, 211117 (2006).
[23]L. Lewin, J. Inst. Electr. Eng. - Part III: Radio Commun. Eng. **94**, 65–68 (1947).
[24]X. Liu, Q. Zhao, C. Lan, and J. Zhou, Appl. Phys. Lett. **103**, 031910 (2013).
[25]A. Andryieuski and A. V. Lavrinenko, Opt. Express **21**, 9144–9155 (2013).
[26]C. Gao and B. Guo, Phys. Plasmas **24**, 093520 (2017).
[27]L. Qi, C. Liu, and S. M. Ali Shah, Carbon **153**, 179–188 (2019).
[28]F. Amiripour, S. Ghasemi, and S. N. Azizi, Appl. Surf. Sci. **537**, 147827 (2021).
[29]H. Dai, L. Yuan, and C. Yin, Phys. Rev. Lett. **124**, 053902 (2020).
[30]M. N. Baitha and K. Kim, J. Appl. Phys. **132**, 053102 (2022).
[31]X. Zhou, X. Ling, H. Luo, and S. Wen, Appl. Phys. Lett. **101**, 251602 (2012).
[32]P. Y. Liu, L. K. Chin, W. Ser, T. C. Ayi, P. H. Yap, T. Bourouina, and Y. Leprince-Wang, Lab Chip **14**, 4237–4243 (2014).
[33]R. Barer and S. Joseph, J. Cell Sci. **s3-96**, 1–27 (1955).
[34]B. Rappaz, P. Marquet, E. Cuche, Y. Emery, C. Depeursinge, and P. J. Magistretti, Opt. Express **13**, 9361–9373 (2005).
[35]R. A. Flynn, B. Shao, M. Chachisvilis, M. Ozkan, and S. C. Esener, Biomed. Microdev. **7**, 93 (2005).